JOURNAL OF OPTOELECTRONICS AND ADVANCED MATERIALS, Vol. 10, No. 10, October 2008, p. 2719 - 2726

Nanostructured transparent and luminescent $Y_2O_3:Eu^{3+}$ thin films

K. M. NISSAMUDEEN, K. G. GOPCHANDRAN*
Department of Optoelectronics, University of Kerala, Kariavattom-695 581, India

Preparation of transparent and photoluminescent Y_2O_3:Eu^{3+} thin films on quartz substrates using pulsed laser deposition technique are reported. Annealing of these films, in the temperature range 973-1073 K, results in enhanced photoemission. The photoemission was found to be maximum for 8 wt.% Eu^{3+} doped Y_2O_3 films, resulting from $^5D_0$–$^7F_2$ transition within europium, emitting red light at 612 nm . The effect of annealing on the structure and morphology of the films are described with XRD, Raman, SEM and AFM. Films annealed at 973 K shows a preferential growth along (222) crystal plane of the cubic Y_2O_3 crystal lattice, and a crystallite size of 49 nm. With increase of annealing temperature, a transition in surface morphology at first from amorphous to nanorods at 773 K and then to nanoislands at 1073 K is described with AFM images. Friction force microscopic images were used to understand the compositional domains on the surface of the films.

(Received April 24, 2008; accepted August 14, 2008)

Keywords: Y_2O_3:Eu, Luminescence, Thin film, Nanostructure

1. Introduction

Luminescent films play an important role in high resolution devices such as cathode ray tubes, electroluminescent devices, plasma display panels and field emission displays [1]. Transparent thin film phosphors (TTFPs) are essential materials in display applications. Improved performance of displays requires high quality phosphors for sufficient brightness and long term stability [2]. To enhance the luminescent characteristics of the phosphors, extensive research has been carried out on rare earth activated oxide phosphors due to their luminescent characteristics, stability in high vacuum, and absence of corrosive gas emission under electron bombardment when compared to currently used sulfide based phosphors. Oxide-based phosphors are likely to emerge as the potential choice for red phosphor in field emission display (FED) [3]. Among those oxide based phosphors, there has been significant research interest in the development of Y_2O_3:Eu^{3+} thin film as one of the most promising red phosphor. Yttrium oxide with Eu^{3+} exhibit strong UV and cathode ray excited luminescence that are useful in lamp and display applications [4]. Photoluminescent and cathodoluminescent thin films of Y_2O_3:Eu^{3+} have potential application in emissive flat-panel displays such as field emission and plasma display panels [5]. Due to $^5D_0$–$^7F_2$ transition within europium, Y_2O_3:Eu^{3+} shows luminescence properties and emits red light of 612 nm wavelength [6]. Thin films are preferred to the traditional discrete powder screens; offer the benefit of light scattering, a reduction of material waste and the potential for fabricating smaller pixel size and to enhance resolution [7]. Dielectric Y_2O_3 film has attracted much attention for its potential application as an electric insulation layer in electroluminescent devices and high-density dynamic random access memory gate dielectrics because of its high band gap (5.8 eV) and large dielectric constant (14 to18) [8]. Europium doped yttrium oxysulfide (Y_2O_2S:Eu), having higher efficiency than Eu-doped yttrium oxide (Y_2O_3:Eu^{3+}), has been used as a traditional cathode ray tube red phosphor [9]. The sulfides, however, are known to degrade rapidly under high current densities needed for field emission display technology [10, 3]. Therefore, oxide-based phosphors are likely to emerge as the material of choice for the FED red phosphor. It is generally accepted that thin film phosphors have certain advantages over bulk-type powder phosphors like better thermal stability, reduced out gassing, better adhesion, and improved uniformity over substrate surface [11]. However, there still remains a fundamental problem in the application of thin-film phosphors (TFP) due to their low brightness in comparison to bulk-type powder phosphors. This can be significantly enhanced by tailoring the surface roughness of TFPs using various methods including variation in processing conditions and modifying TFP surface [12]. The increase in roughness of these films due to annealing is attributed to the enhanced grain size [13]. The resolution of images in display devices is related closely to the particle size of phosphor used. Smaller particles are favorable for higher resolution. The advances made in the reduction of the size of electronic devices require the investigation of the physical properties of materials with particle size in nanometer regime [14, 15]. Due to the low excitation voltage, electron penetration into the luminescent particles is very shallow. This means that

the effective luminescent region may be confined near the surface of particles and that the low voltage excitation favors small particles or large specific surface area. As a result, the small size of nanoparticles allows complete penetration by low-voltage electrons for efficient material utilization. Yttrium oxide films have been grown mainly using electron-beam evaporation [16] and radio frequency sputtering [17- 19]. Pulsed laser deposition (PLD) has recently been used for the growth of yttrium oxide films, which provides a unique process for stoichiometric evaporation of target materials and control of film morphology [20, 21]. In the present study an attempt has been made to prepare transparent Y_2O_3:Eu^{3+} thin film phosphor using pulsed laser ablation technique and to improve the intensity of photoemission through annealing process.

2. Experimental procedures

Europium doped yttrium oxide thin films were fabricated on amorphous fused quartz substrates by pulsed laser deposition (PLD) technique, using a Q-switched Nd:YAG laser, (Quanta-ray INDI-Series, Spectra-Physics) with 12 J/cm^2 of laser energy density at 532 nm, pulse width 7 ns, and repetition frequency 10 Hz. The target–substrate distance was 6.5 cm and the deposition time was 30 minutes. The target was rotated with constant speed to avoid pitting of the target at any given spot and to obtain uniform ablation. The Y_2O_3 and Eu_2O_3 target was prepared from yttrium oxide and europium oxide powder of 99.99% purity (Sigma-Aldrich). The powder target was isostatically pressed and sintered at 1623 K for 4 h, to form pellets of diameter 1.4 cm. The Y_2O_3:Eu^{3+} films with different europium concentration were fabricated at room temperature under a vacuum of 10^{-6} mbar and subsequently annealed at different temperatures up to 1073 K, for duration of 1 h. The heat treatment consisted of raising the temperature at a rate of 5 K min^{-1}, then maintaining the temperature for 1 h and gradually lowering it to room temperature at the rate of 0.8 K min^{-1}. The structure and crystallanity of the films were investigated by X-ray diffraction (XRD), using an X'per PRO diffractometer (PANalytical), operated with Cu Kα radiation source (λ = 0.15406 nm, 40 kV, 30 mA). The surface morphology and roughness of the films were investigated by atomic force microscopy (AFM), using Molecular imaging Pico Plus with friction force microscopy (FFM) and scanning electron microscopy (SEM), using a FEI Quanta 200 system. Lateral force microscopy (LFM) also known as friction force microscopy (FFM) is a derivative mode of contact mode AFM, in which the tip is constantly in contact with the sample surface. Hence, in addition to the near-vertical deflection signal which is usually present during contact mode, the detector can also collect a sizeable lateral deflection signal from the cantilever's twisting motion. The strength of the lateral deflection signal is related to the friction force between the sample surface and the tip. In this mode, signal is highly susceptible to topography variations; the rougher the sample surface, the more topography convolution. In order to overcome this convolution, to decipher the variation in friction force from the topography, two LFM images are often captured adjacently. One of these two images is constructed from the detector signal during the trace of each round-trip cycle and the other, during retrace. Then one of the two images is inverted and subtracted from the other. This reduces the topographic artifact in the signal. Photoluminescence (PL) studies were done by using Fluorolog-III spectroflurophotometer with optimum excitation wavelength. Optical measurements were performed in the wavelength range from 200 to 900 nm, using a double beam UV–Vis spectrophotometer, Jasco-V 550.

3. Results

In this work optimization of the films was done based on the enhancement in photoemission as a function of europium concentration and annealing temperature. PL intensity of 8 wt.% Eu^{3+} doped Y_2O_3 films were found to be maximum compared to other Eu^{3+} concentrations. Figure 1 shows the XRD patterns of these films annealed at different temperatures. The XRD patterns of the films deposited at room temperature and annealed at lower temperatures showed no significant peak indicating amorphous like nature of the films. The XRD patters are indexed according to JCPDS data card (No: 41-1105) of cubic structure of Y_2O_3. No peaks correspond to europium or its compounds are found in the patterns indicating substitution of europium ions in yttrium sites. The crystallite size was determined from the most significant peaks, using Scherrer's equation,

$$D_{hkl} = \frac{0.9\lambda}{\beta_{hkl}\cos(\theta_{hkl})} \quad (1)$$

where λ is the X-ray wavelength, θ_{hkl} is the Bragg diffraction angle and β_{hkl} is the full width at half maximum (FWHM) of the peak in radians in the X-ray diffraction pattern. The film annealed at 973 and 1073 K showed grain size of 49 and 54 nm respectively indicating that the grains grow in size with temperature. For the nanophosphors, the growth in grain size and the decrease in the surface area of the particles may increase the luminescence emission, because of the reduction of surface defects and the nonradiative rates [22, 23].

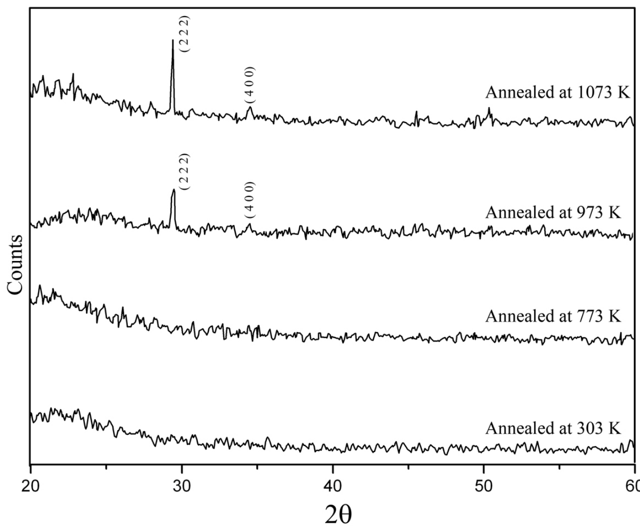

Fig.1. XRD patterns of $Y_2O_3:Eu^{3+}$ (8 wt %) films annealed at different temperatures.

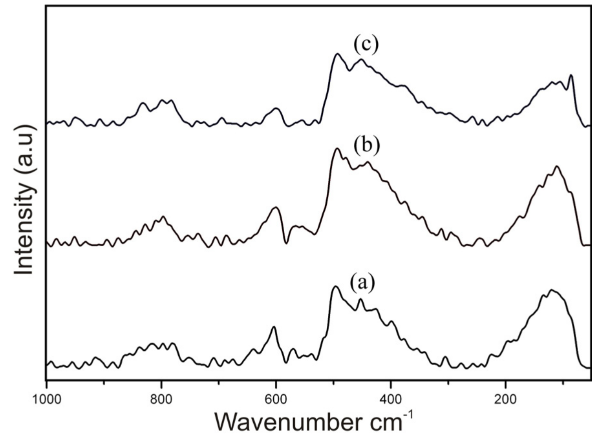

Fig. 2. FT-Raman spectra of $Y_2O_3:Eu^{3+}$ (8 wt %) films: (a) as deposited; annealed at (b) 973 and (c) 1073 K.

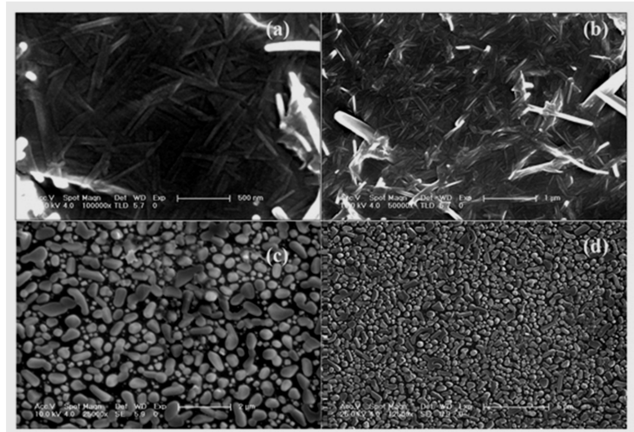

Fig.3. SEM images of $Y_2O_3:Eu^{3+}$ (8 wt %) films annealed at (a&b) 773 and (c&d) 1073 K.

Y_2O_3 crystallizes in the cubic system Ia3 (Th7) with four formula units in the primitive unit cells. The 54 Raman active optical modes are distributed under the irreducible representations [24] as

$$\Gamma = 4Ag + 4Eg + 14Fg \qquad (2)$$

Here A is non-degenerate, E is doubly degenerate and F is triply degenerate. As expected [25], the Raman bands due to Y_2O_3 are observed in the region 120-600 cm^{-1} region. The band observed in the region 770-800 cm^{-1} is due to the Eu^{3+} doping. The change of the most intensive Raman band from 378 cm^{-1} [26] to two spilt components in the region 440-500 cm^{-1} as shown in the figure 2, is due the strain induced on the surface by Eu^{3+} doping. The intensity variation, shifting and splitting observed for the low frequency band in the region 80-120 cm^{-1} indicates changes in the lattice parameter with change in annealing temperature [2]. The highest frequency observed for Y_2O_3 around 600 cm^{-1} which corresponds to Fg + Ag modes is temperature sensitive. At 1073 K a single band is observed for this mode as reported by Zhang et al [2]. The as deposited sample has three bands in this range indicating a lifting of degeneracy of the Fg mode. At 773 K two bands are observed, one for Fg and other one being the Ag mode. The lattice parameters determined from the XRD pattern shown in the figure 1 is 1.05757 nm and 1.05868 nm for the film annealed at 973 K and 1073 K respectively. This change in lattice parameter agrees with the observations made in Raman spectra.

Fig. 3 shows the SEM micrographs of the films annealed at 973 and 1073 K. The atomic force and friction force microscopic images along with section analysis are shown in figure 4 and 5. The morphology of the as deposited film exhibits an amorphous nature. The film annealed at 773 K shows formation of nanorods. The AFM image (figure 4(b)) of this film is a replica of the SEM image shown in figure 3 (a) and is an indication of the uniform distribution of nanorods on the entire surface of the film. Further increase of annealing temperature results in transformation of this to an island like morphology with voids between islands as seen in SEM and AFM images (figure 3(c) and 4(c)) and is found to be highly crystalline with preferential growth along (222) crystal plane. Depending on the properties and fabrication route, the crystal boundaries are associated with various degrees of structural and compositional disorder [26]. After the types and morphology of the phases present, grain size is an obvious and important microstructural characteristic which has a significant effect on properties of the films. Grain boundaries are local regions of relatively high energy; they often act as nucleation sites for phase transformations. The spontaneous ordering of

nanostructures has established that long-range elastic interaction is the driving force for ordering [27]. However, details of ordering of such arrays are subject of much debate (involving thermodynamic and kinetic considerations) [28]. From thermodynamic standpoint, grain boundaries increase the total energy of a material. Therefore there is a tendency to reduce the total amount of grain boundary area, since large grains have less grain boundary area per unit volume than small grains. The grain growth could achieve a reduction in the energy associated with grain boundaries. On the other hand, annealing of films at elevated temperatures results in enhanced oxidation kinetics. The FFM images shown in the figure 5 depict the compositional domains in the morphology with high lateral resolution [29]. The roughness of the films is also found to increase with annealing temperature. The average roughness of these films, measured by the AFM, was found to increase from 1.054 to 4.661 nm due to annealing. The increase in roughness due to annealing is attributed to the enhanced grain size.

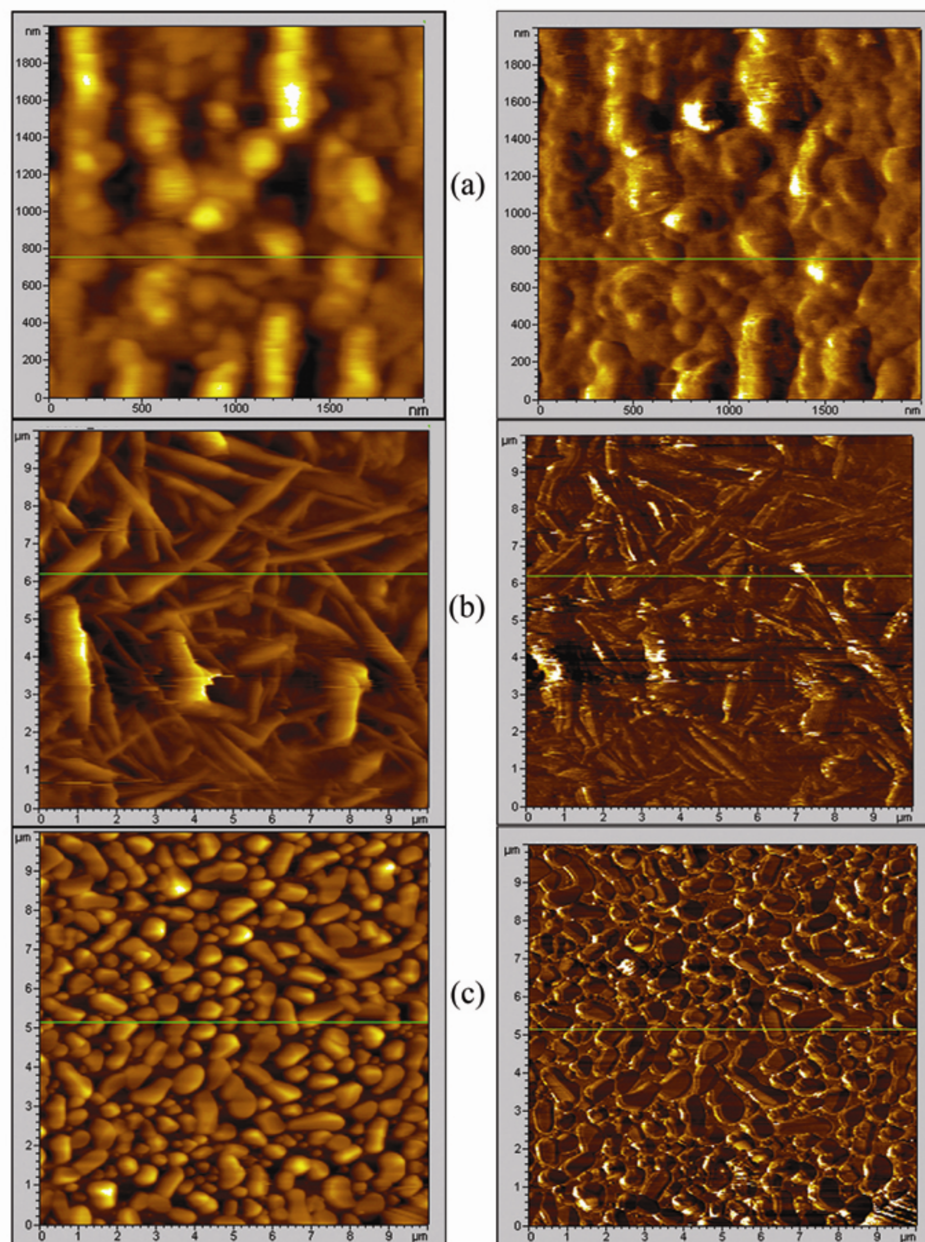

Fig.4. AFM images in 2D along with FFM images of $Y_2O_3:Eu^{3+}$ (8 wt %) films: (a) as deposited; annealed at (b) 773 and (c) 1073 K.

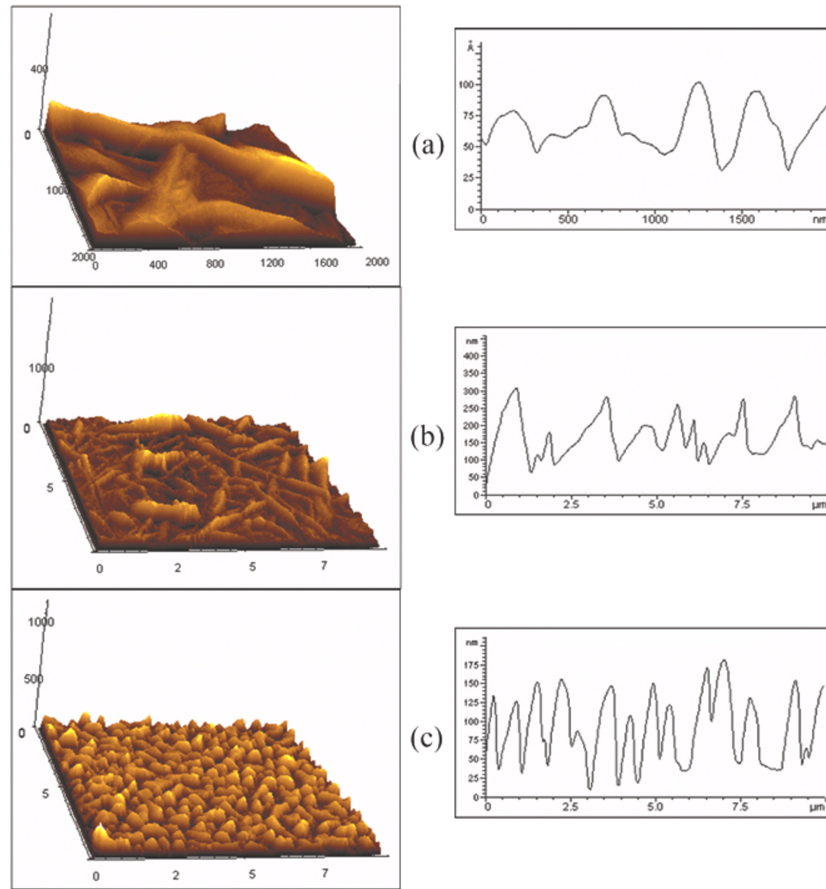

Fig. 5. AFM images in 3D along with section analysis of $Y_2O_3:Eu^{3+}$ (8 wt %) films: (a) as deposited; annealed at (b) 773 and (c) 1073 K.

Fig. 6(a) shows the plots of PL spectra of $Y_2O_3:Eu^{3+}$ films annealed at 1073 K with different europium concentrations. It can be seen that photoemission intensity is maximum for 8 wt. % Eu^{3+} doped Y_2O_3 films compared to other doping concentrations. Figure 8(b) shows the plots of PL spectra of 8 wt. % Eu^{3+} doped Y_2O_3 films with different annealing temperatures. The spectra exhibit optical properties of Eu^{3+} ions in the cubic Y_2O_3 host structure. The emission spectrum shows transitions from excited $^5D_0$ state to ^7F_J (J=0, 1, 2, 3, 4) levels of the Eu^{3+} ion. The weak emission peaks present in the 580 to 600 nm region, of the photoluminescence spectra can be attributed to the $^5D_0 \rightarrow {}^7F_1$ magnetic dipole transition[31]. Due to $^5D_0$–$^7F_2$ transition within europium, $Y_2O_3:Eu^{3+}$ shows luminescence properties and found to emit intense red light at 612 nm and a low intense emission at 630 nm region as observed by other researchers [32, 33]. In addition, weak emission peaks for the $^5D_0 \rightarrow {}^7F_3$ transition is observed at 653 nm and $^5D_0 \rightarrow {}^7F_4$ transition is observed at 710 nm [34, 35]. The observed optical transition within $4f^{\,n}$ configuration are mainly attributed to electric dipole transitions, which are forced by the odd parity components of the crystalline electric field. For C_{3i} symmetry the parity of the electron wave function is an exact quantum number ($4f^{\,6}$ is even) and only magnetic dipole transitions should be observed. For these transitions, the selection rule ΔJ = 0, 1 (J =0 $\rightarrow$ J = 0 forbidden) holds true. For the $^5D_0$–$^7F_1$ transition of the Eu^{3+} ion in the cubic structure, five emission peaks should be present: two peaks that are attributed to Eu^{3+} ions residing in C_{3i} sites and three peaks for Eu^{3+} in C_2 sites [36]. It can be seen from photoluminescence spectra shown in figure 8, $Y_2O_3:Eu^{3+}$ films subjected to annealing at 1073 K has maximum intensity. Figure 9 shows the variation of PL intensity of $Y_2O_3:Eu^{3+}$ films as a function of annealing temperature. The PL intensity and average roughness have similar behaviors as a function of annealing temperature. The increase in annealing temperature from 303 to 1073 K resulted in an increase in surface roughness which in turn increased the PL intensity. The improvement in PL performance may be attributed to reduced internal reflections caused by rougher surfaces. The light generated in the films is reflected and transmitted at film-substrate and film-air –interfaces. The scattering at the film-air interface has two components: a specular component and a diffuse scattering component. The diffuse scattering component depends on the surface roughness of the film [20].

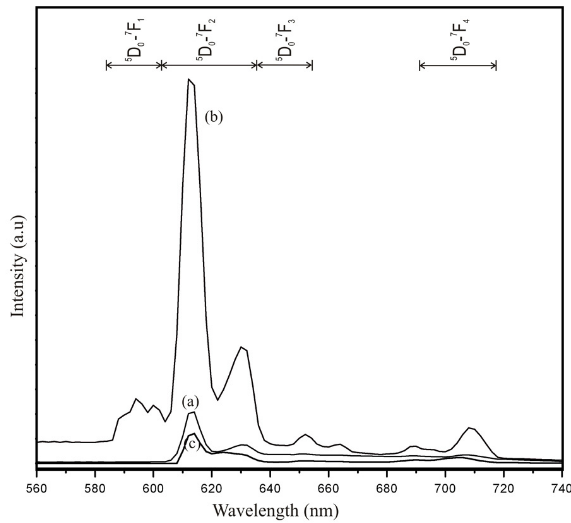

Fig.6(a). PL spectra of Y_2O_3:Eu^{3+} films annealed at 1073 K (a) 4, (b) 8 and (c) 12 wt %.

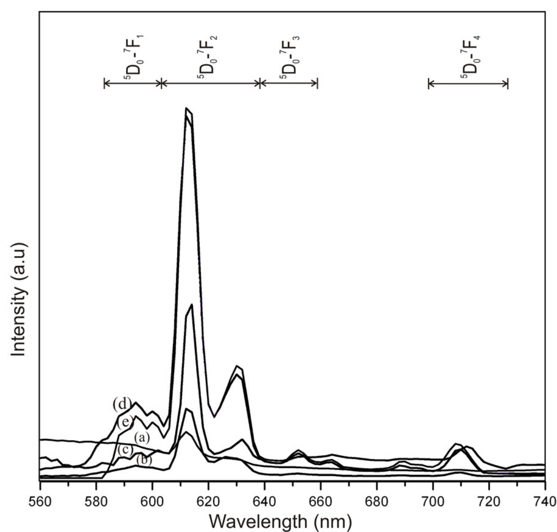

Fig. 6(b). PL spectra of Y_2O_3:Eu^{3+} (8 wt %) films: (a) as deposited; annealed at (b) 773, (c) 873 (d) 973 and (e) 1073 K.

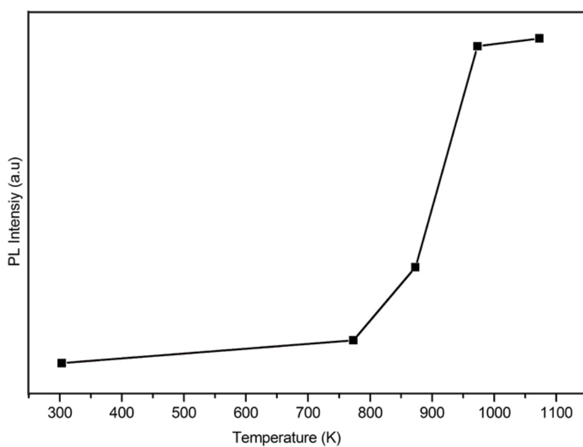

Fig.7. Variation of PL intensity with annealing temperature of Y_2O_3:Eu^{3+} (8 wt %) films.

Fig. 8 shows transmission spectra of the as deposited and annealed Y_2O_3:Eu^{3+} films at different temperatures, in the wavelength ranging from 200 to 800 nm. The transmittance of the film is found to be sensitive to annealing temperature. The optical constant like refractive index (n), film thickness (t) and optical band gap energy (Eg) of the films are determined from the transmission spectrum and is given in table 1. 1n the region of weak and medium absorption, where $\alpha \neq 0$, the transmittance decreases mainly because of the effect of (α) and refractive index (*n*) and is given by,

$$n = \left[N + \left(N^2 - s^2\right)^{1/2} \right]^{1/2} \tag{3}$$

Where

$$N = \left\{ \frac{2s(T_M - T_m}{T_M T_m} \right\} + \frac{s^2+1}{2} \tag{4}$$

here *s* is the refractive index of the substrate and T_M and T_m are the transmission maximum and transmission minimum of the envelope functions, respectively. By solving equation (3) the refractive index of two consecutive maxima or minima can be obtained. For determining the film thickness (t) these values are subsequently used in the following relation,

$$t = \frac{\lambda_1 \lambda_2}{2(n_1\lambda_1 - n_2\lambda_2)} \tag{5}$$

quantitative values of band gap energy (E_g) can be evaluated using the relation [38],

$$\alpha = \frac{A}{h\nu}(h\nu - E_g)^\eta \tag{6}$$

where A is a constant, hν is the incident photon energy, and the exponent η depends on the kind of optical transition. For crystalline semiconductors, the values of η can be 1/2, 3/2, 2, or 3 depending on the transitions are direct allowed, direct forbidden, indirect allowed and indirect forbidden transitions, respectively [37]. The value of η = 2 for the indirect allowed transition is found to be most suitable for these films, since it gives the best linear graph in the band edge region. By extrapolating the linear portion to the photon energy axis, the value of band gap can be obtained. The value of band gap is found to be maximum for the film annealed at 973 K.

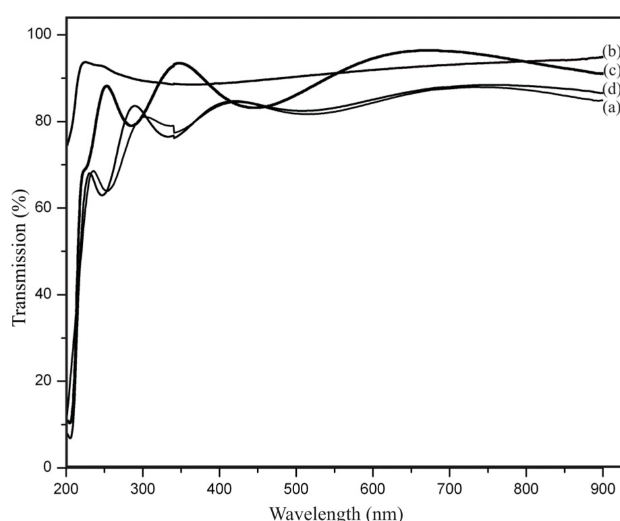

Fig.8. Transmittance spectra of Y_2O_3:Eu^{3+} (8 wt %) films: (a) as deposited; annealed at (b) 773.

Table 1. Refractive index (n), film thickness (t), and optical band gap (E_g) of Y_2O_3:Eu^{3+} (8 wt %)films annealed at different temperatures

Annealing temp. (K)	Thickness (*t*) (nm)	Refractive index (*n*)	Transmittance at 612 nm (%)	Band gap (*Eg*) (eV)
303	401	2.008	85.01	5.01
773	393	2.051	92.04	5.45
973	390	2.071	95.36	5.43
1073	376	2.135	85.75	5.37

4. Conclusion

In summary, nanostructured high-quality Y_2O_3:Eu^{3+} transparent thin-film phosphors have been deposited on fused amorphous quartz substrate using a PLD technique. The effect of annealing, on the structure and morphology of the films are described with XRD, Raman, SEM and AFM. Annealing of the 8 wt% Eu doped films, in the temperature range 973-1073 K, shows high photoemission at 612 nm and an average transmittance above 85% in the visible region. The improvement in photoemission from annealed films can be attributed to improved crystallanity, and reduced internal reflections caused by rougher surfaces. The PL intensity and roughness have shown similar behaviors as a function of annealing temperatures.

References

[1] J. Y. Choe, D. Ravichandran, S. M. Blomquist, D. C. Morton, K. W. Kirchner, M. H. Ervin, U. Lee, Appl. Phys. Lett. **78**, 3800 (2001).
[2] K. Zhang, A. K. Pradhan, B. George, L. U. N. Roy, Y. Cui, A. Burger, J. Opt. Soc. Am. B **21**, 1804-08 (2004).
[3] H. C. Swart, J. S. Sebastian, T. A. Trottier, S. L. Jones, P. H. Holloway, J. Vac. Sci. Technol. A **14**, 1697 (1996).
[4] Q. Y. Zhang, K. Pita, S. Buddhudu, C. H. Kam, J. Phys. D: Appl. Phys. **35**, 3085–3090 (2002).
[5] G. A. Hirata, J. McKittrick, M. A. Borja, J. M. Siqueiros, D. Devlin, Appl. Surf. Sci. **113/l 14**, 509-514 (1997).
[6] K. A. Wickersheim, R. A. Lefever, J. Electrochem. Soc. **111**, 47 (1964).
[7] J. McKittrick, C. F. Bacalski, G. A .Hirata, K. M. Hubbard, S. G. Pattillo, K. V. Salazar, M. Trkula, J. Am. Ceram. Soc. **83**, 1241(2000).
[8] J. H. Jeong, J. S. Bae, S. S. Yi, J. C. Park, Y. S. Kim, J. Phys. Condens. Matter **15**, 567–574 (2003).
[9] J. D. Kingsley, G. W. Ludwig, J. Electrochem. Soc. **117** 353 (1970).
[10] S. Itoh, T. Kimizuka, T. Tonegawa, J. Electrochem. Soc. **136**, 1819 (1989).
[11] S. S. Kim, J. H. Moon, B.T. Lee, K. S. Sohn, T. S. Kang, J. H. Je, Appl. Surf. Sci. **221**, 231-236 (2004).
[12] R. K. Singh, Z. Chen, D. Kumar, K. Cho, M. Ollinger, Appl. Surf. Sci. **197-198** 321-324 (2002).
[13] G. Gang, P. P. Ong, C. Chen, S. Roth, J. Phys. D: Appl. Phys. **33**, 1263–1266. (2000).
[14] H. Song, B. Chen, H. Peng, J. Zhang, Appl. Phys. Lett. **81**, 1776-1778 (2002).
[15] S. J. Hong, M. G. Kwak, J. Han, J. Korean Physical Soc.**45**, 721-724 (2004).
[16] R. N. Sharma, S. T. Lakshami Kumar, A. C. Rastogi Thin Solid Films, **199**, 1 (1991).
[17] A. F. Jankowski, L. R. Schrawyer, J. P. Hayes, J. Vac. Sci. Technol. A **11**, 1548 (1993).
[18] K. Onisawa, M. Fuyana, K. Tamura, K. Taguchi, T. Nakayama, Y. Ono, J. Appl. Phys. **68**, 719 (1990).
[19] W. M. Cranton, D. M. Spink, R. Stevens, C. B. Thomas, Thin Solid Films **226**, 156 (1993).
[20] R. K. Singh and J. Narayan, Phys. Rev. B **41**, 8843 (1990).
[21] J. A. Greer and M. D. Tabat, J. Vac. Sci. Technol. A **13** 1175 (1995).
[22] Q. W. Chen, Y. Shi, J. Y. Chen, J. L. Shi, J. Mater. Res. **20**, 1409 (2005).
[23] L. Xu, BoWei, Z. Zhang, Zhe L¨u, HongGao, Y.Zhang, Nanotechnology **17**, 4327 (2006).
[24] Y. Repelin, C. Proust, E. Husson, J. M. Beny, J. Solid state chem.**118**, 163 (1995).
[25] T. Ming-hua, T. Yi-chun, X u e - j u n Z, Y. A. Zhi, C. Chuan-pin, H. U. Zeng-shun Trans. Nonferrous Met. Soc. China, **16**, s63 (2006).
[26] B. Sasi, K. G. Gopchandran, Nanotechnology **18**, 115613 (2007).

[27] V. A. Schhukin, D. Bimberg, Rev. Mod. Phys. **71**, 1125 (1999).
[28] S. Aggarwal, A. P. Monga, S. R. Perusse, R. Ramesh, V. Ballarotto, E. D. Williams, B. R. Chalamala, Y. Wei, R. H. Reuss, Science **287**, 2235 (2000).
[29] Koichiro Iwahori, Shunji Watanabe , Maki Kawai, Keisuke Mizuno, Kenji Sasaki, Mamoru Yoshimoto J. Appl. Phys. **88**, 7099 (2000).
[30] I. Horcas, J. M. Fernandez, J.Gomez-Roderiguez, J. Colchro, Gomez-Herrero, A. M. Baro, Rev. Sci. Inst. **78,** 13705 (2007).
[31] J. Dhanaraj, R. Jagannathan , T. R. N. Kutty, Chung-Hsin Lu, J. Phys. Chem. B **105**, 11098 (2001).
[32] Z. Qiu, Y. Zhou, Mengkai L¨u, J. Zhou, A. Zhang, Z. Yang, Q. Ma, Nanotechnology **18**, 495705 (2007).
[33] J. Lian, L. Yang, X. Y. Chen, G. K. Liu, L. M. Wang, R. C. Ewing, D. Shi Nanotechnology **17**, 1351 (2006).
[34] M. Darbandi, W. Hoheise, T. Nann, Nanotechnology **17**, 4168 (2006).
[35] D. Kumar, K. G. Cho, Zhan Chen, V. Craciun, P. H. Holloway, R. K. Singh, Phys. Rev. B **60**, 1333 (1999).
[36] H. S. Nalwa, L. S. Rohwer, Handbook of Luminescence, Display Materials and Devices, American Scientific Publishers –USA (2003).
[37] J. I. Pankove, Optical Processes in Semiconductors, *Dover* Publications, New York. (1971).

*Corresponding author: gopchandran@yahoo.com